Supplementary Information

Dean M. Sweeney, Bolton Tran, and Bryan R. Goldsmith*

Department of Chemical Engineering, University of Michigan, Ann Arbor, MI

E-mail: bgoldsm@umich.edu

Dopant Segregation and Aggregation in JDFTx

All DFT calculations for the segregation and aggregation studies were completed using the Joint Density Functional Theory Software (JDFTx) with the Revised Perdew-Burke-Ernzerhof Functional. A plane wave energy cutoff of 544 eV was used for valence electron expansion, while the core electrons were accounted for using the projected augmented wave potentials. Spin-polarized calculations were done for Ni_1Cu only. Each structure was modeled using a $3 \times 3 \times 5$ unit cell with 4 relaxed layers and 1 frozen layer. A surface atom in the Cu host metal (computed lattice constant: 3.70 Å) was replaced by the dopant atom(s) to simulate the SAA structure. For aggregation studies, an adjacent Cu atom on the surface layer was replaced by the dopant(s). For segregation studies, a Cu atom in the third layer was replaced by the dopant atom(s) while the surface layer was pure Cu. The Brillouin zone was sampled with a $4 \times 4 \times 1$ Monkhorst–Pack k-point grid. Periodic images in the z-direction were separated by a vacuum layer of 15 Å to minimize periodic interactions. All adsorbates and the four topmost layers of the surface slab model were relaxed by geometry optimization, with forces converged to <0.01 eV/Å. This methodology was benchmarked with the results of Darby et al., as shown in Figure 1.[1]

For computing grand free energies, we used the CANDLE implicit solvation model to simulate solvent and ion effects. To simulate an applied potential, we set the electronic Fermi

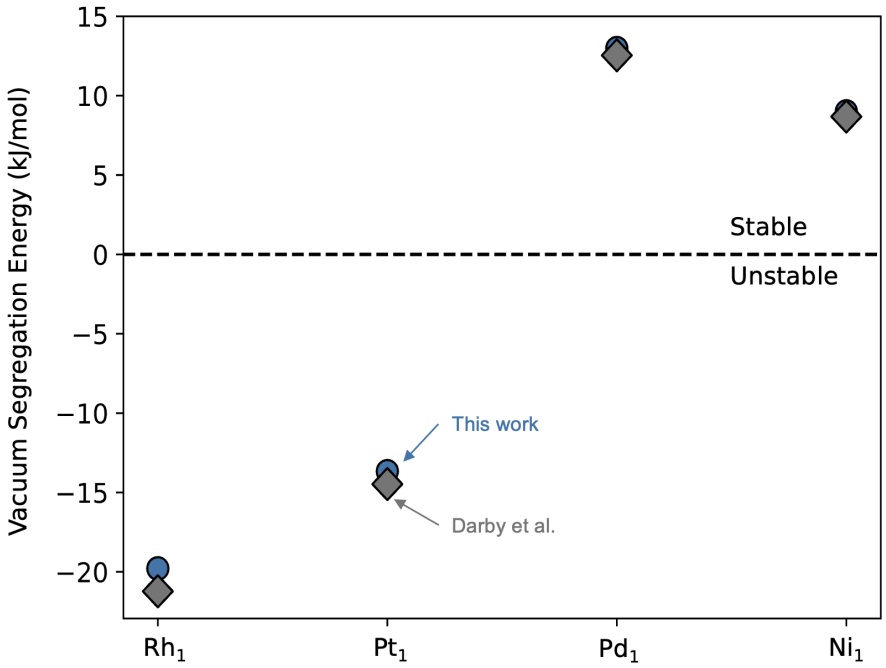

Figure 1: Dopant segregation energies calculated in vacuum compared to the work of Darby et al.[1] X_1Cu SAAs are labeled inset as X_1.

energy (equal to the electrochemical potential of an electron, μ_e) to the target potential, which was converted to the SHE scale via $U_{\text{SHE}} = \frac{-\mu_e - \phi_{\text{ref}}}{e}$. In this work, $\phi_{\text{ref}} = 4.66$ V, as calibrated to the CANDLE implicit solvation model.

Segregation energies and aggregation energies for bare surface slabs (without adsorbates present) are calculated via eqs. (1) and (2) and shown in Table 1. In these equations Φ_{Cu}, Φ_{SAA}, Φ_{dimer}, and Φ_{bulk} are the grand free energies of the surface with just Cu, a single dopant (SAA), clustered dopants (dimer), or when the dopant is in the subsurface (bulk). The partial charges for all dopants are shown in Figure 2.

$$\Delta\Phi_{\text{seg}} = \Phi_{\text{bulk}} - \Phi_{\text{SAA}} \tag{1}$$

$$\Delta\Phi_{\text{agg}} = \Phi_{\text{dimer}} + \Phi_{\text{Cu}} - 2\Phi_{\text{SAA}} \tag{2}$$

Table 1: Bare slab segregation and aggregation energies computed from explicit GC-DFT (units: kJ/mol)

	$\Delta\Phi_{seg}(-0.114\ V)$	$\Delta\Phi_{seg}(-0.714\ V)$	$\Delta\Phi_{agg}(-0.114\ V)$	$\Delta\Phi_{agg}(-0.714\ V)$
Ti_1Cu	–2.58	–18.61	12.93	12.35
Ni_1Cu	–20.12	–19.22	–1.23	–1.37
Nb_1Cu	–21.52	–29.07	–59.95	–57.07
Ru_1Cu	–32.62	–30.11	–35.87	–36.40
Rh_1Cu	–13.70	–11.75	4.75	4.26
Pd_1Cu	13.27	14.35	10.89	10.72
Pt_1Cu	9.90	12.84	13.13	13.00
Au_1Cu	50.95	53.05	13.81	14.09

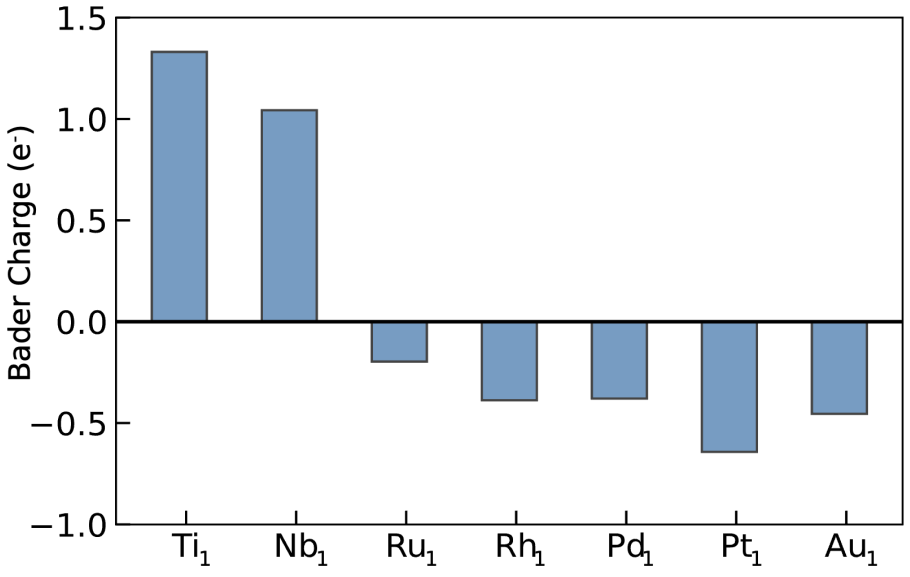

Figure 2: Bader charge analysis on the studied SAAs under -0.114 V vs SHE as computed in JDFTx. X_1Cu SAAs are labeled inset as X_1.

Segregation energies and aggregation energies for H* and NO_3* are calculated via eqs. (3) and (4) shown in Tables 2 and 3. In these equations, $\Delta\Phi^{(A^*)}_{\text{ads, Cu}}$, $\Delta\Phi^{(A^*)}_{\text{ads, SAA}}$, and $\Delta\Phi^{(A^*)}_{\text{ads, Dimer}}$ represent the adsorption free energies of an adsorbate, A*, on a pure Cu site, a SAA site, and a dimer site. Note that when taking the difference in adsorption energies for a given adsorbate, the reference states for each adsorption energy will automatically cancel out.

$$\Delta\Phi^{(A^*)}_{\text{seg}} = \Delta\Phi_{\text{seg}} + (\Delta\Phi^{(A^*)}_{\text{ads, Cu}} - \Delta\Phi^{(A^*)}_{\text{ads, SAA}}) \tag{3}$$

$$\Delta\Phi^{(A^*)}_{\text{agg}} = \Delta\Phi_{\text{agg}} + (\Delta\Phi^{(A^*)}_{\text{ads, Dimer}} - \Delta\Phi^{(A^*)}_{\text{ads, SAA}}) \tag{4}$$

Table 2: H* segregation and aggregation energies computed from explicit GC-DFT (units: kJ/mol)

	$\Delta\Phi^{\text{H*}}_{\text{seg}}(-0.114\text{ V})$	$\Delta\Phi^{\text{H*}}_{\text{seg}}(-0.714\text{ V})$	$\Delta\Phi^{\text{H*}}_{\text{agg}}(-0.114\text{ V})$	$\Delta\Phi^{\text{H*}}_{\text{agg}}(-0.714\text{ V})$
Ti_1Cu	9.02	–0.52	–6.30	–14.35
Ni_1Cu	–1.90	–0.89	–14.32	–13.44
Nb_1Cu	–1.90	–6.12	–68.16	–78.83
Ru_1Cu	–2.32	0.46	–28.13	–29.06
Rh_1Cu	7.19	9.62	–1.69	–2.35
Pd_1Cu	15.41	17.21	7.02	6.64
Pt_1Cu	16.66	19.23	9.25	9.36
Au_1Cu	30.55	31.93	29.64	30.28

Table 3: NO_3^* segregation and aggregation energies computed from explicit GC-DFT (units: kJ/mol)

	$\Delta\Phi_{seg}^{NO_3^*}(-0.114\ V)$	$\Delta\Phi_{seg}^{NO_3^*}(-0.714\ V)$	$\Delta\Phi_{agg}^{NO_3^*}(-0.114\ V)$	$\Delta\Phi_{agg}^{NO_3^*}(-0.714\ V)$
Ti_1Cu	79.63	75.81	–60.90	–73.48
Ni_1Cu	–4.06	–5.06	–13.95	–11.86
Nb_1Cu	75.45	69.75	–133.32	–141.30
Ru_1Cu	-4.05	–3.00	-58.80	–53.16
Rh_1Cu	–5.44	–3.40	–2.77	-0.24
Pd_1Cu	4.88	8.95	17.62	14.17
Pt_1Cu	–9.87	–5.83	31.06	-
Au_1Cu	25.32	-	-	-

The adsorption configurations of NO_3^* on the SAA sites as optimized from GC-DFT is shown in Figure 3. The configuration of NO_3^* on Ti_1Cu and Nb_1Cu indicates that the molecule interacts strongly with the Ti_1 and Nb_1 sites over Cu. Conversely, the configuration of NO_3^* on Au_1Cu indicates that it interacts weakly with the Pt_1 and Au_1 sites.

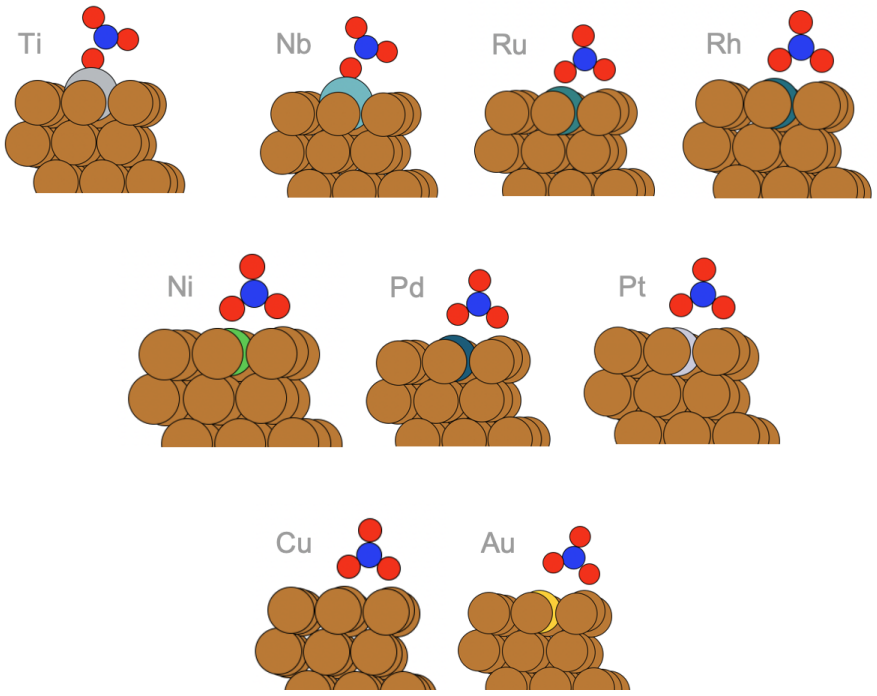

Figure 3: Adsorption configurations for NO_3^* optimized with GC-DFT for all SAAs.

Potential Dependence of Nitrate Adsorption and Dissociation

Thermodynamic Cycle for Nitrate Adsorption

DFT cannot accurately calculate the free energy of an aqueous-phase anion (NO_3^-). Therefore, the energy change from state zero to state four (ΔG_{04}) must be computed with a different thermodynamic cycle, shown below.

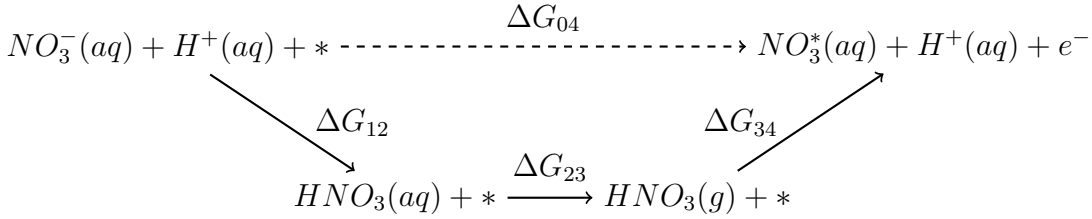

The first reaction step (ΔG_{12}) represents the proton association-dissociation equilibrium of nitric acid, of which free energy change can be obtained from its pKa (-1.28).[2] Reaction step two (ΔG_{23}) represents the de-solvation process of nitric acid, of which free energy change can be obtained from its Henry's constant (2100 $\frac{\text{mol}}{\text{m}^3\cdot\text{Pa}}$).[3] At 1 mol/L solution standard state (1 bar, 298 K), ΔG_{12} and ΔG_{23} are 0.08 $\frac{\text{eV}}{\text{V}}$ and 0.40 $\frac{\text{eV}}{\text{V}}$, respectively. For step three (ΔG_{34}), we applied the CHE model to rewrite $H^+(aq) + e^-$ as $\frac{1}{2}H_2$ at 0.0 V vs SHE and pH=0. Other energies, including gas phase HNO_3 and H_2 as well as the bare slab and slab with NO_3^*, can be computed with DFT and thermochemistry corrections. Hence, to compute the grand free energy of NO_3^- adsorption at any pH and potential, we utilized eq. (5). Note that we are using $\Phi(U)$ to represent grand free energies and G to represent non-potential dependent free energies. Additionally, in this work, we compute $\Delta\Phi_{\text{ads}}^{\text{NO}_3{}^*}(U)$ at a pH of 0.0 since it is trivial to shift the energies by a constant.

$$\Delta\Phi_{\text{ads}}^{\text{NO}_3{}^*}(U) = \Phi_{\text{NO}_3{}^*}(U) - \left(\Phi_{\text{slab}}(U) + G_{\text{HNO}_3} - \frac{1}{2}G_{\text{H}_2}\right) - eU - 0.0592\text{pH} + \Delta G_{03} \quad (5)$$

DFT Calculations: JDFTx and VASP

All DFT calculations for both the CHE model and the analytical GC-DFT method were completed using the Vienna Ab Initio Simulation Package (VASP) with the Revised Perdew-Burke-Ernzerhof Functional. A plane wave energy cutoff of 544 eV was used for valence electron expansion, while the core electrons were accounted for using the projected augmented wave potentials. Spin-polarized calculations were done for Ni only. We found that Ni_1Cu energetics and system properties did not change with and without spin-polarization. Each structure was modeled using a $3 \times 3 \times 4$ unit cell with 2 relaxed layers. Pure metal lattice constants were computed and used to generate each slab.

For SAAs, a surface atom in the Cu host metal (computed lattice constant: 3.70 Å) was replaced by the dopant atom(s) to simulate the SAA structure. The Brillouin zone was sampled with a $4 \times 4 \times 1$ Monkhorst–Pack k-point grid. Periodic images in the z-direction were separated by a vacuum layer of 15 Å to minimize interactions. All adsorbates and the two topmost slab layers were relaxed by geometry optimization, with forces converged to $<$0.01 eV/Å. For transition state searches, we used the Climbing Image Nudge Elastic Band method (CI-NEB) with forces converged to $<$0.05 eV/Å. All transition states were confirmed to have one large imaginary frequency corresponding to the N-O bond dissociation. Enthalpic and entropic thermochemistry corrections for H_2(g), HNO_3(g), adsorbed nitrate in solution, and nitrate dissociation barriers were computed using the rigid rotor harmonic oscillator approximation as implemented in the Atomic Simulation Environment (ASE).

Computing Parameters for aGC-DFT

To generate the data for the analytical GC-DFT model, all simulations were converged in both vacuum and solvent, according to the original work of Argawal et al.[4] Surface normal dipole moments were extracted from converged vacuum simulations within VASP (LDIPOL=.TRUE.). To compute the polarizability, we performed single-point calculations (starting from the vacuum-optimized structure) under different EFIELD values of 0.0 V to

0.6 V. We then fit a second-order polynomial to the computed energies as a function of the electric field. The polarizability was determined from the coefficient of the second-order term in the best-fit polynomial. Surface normal dipole moments and polarizabilities are included in the accompanying data file.

To compute grand free energies explicitly in JDFTx for nitrate adsorption and dissociation over Cu(111), we utilized identical settings (i.e., functional, k-points, energy cutoff, ... etc.) as those specified in VASP. Cu(111) was modeled using a 3 × 3 × 4 unit cell with 2 relaxed layers. Solvent effects were accounted for with the CANDLE implicit solvation model. Applied potentials were simulated according to the methodology outlined previously. The electrosorption valency, shift in dipole moment, and charge transfer for nitrate adsorption are shown in Table 4. The symmetry factor and shift in dipole moment for nitrate dissociation are shown in Table 5. All other data not included here or the main text can be found within the accompanying data file.

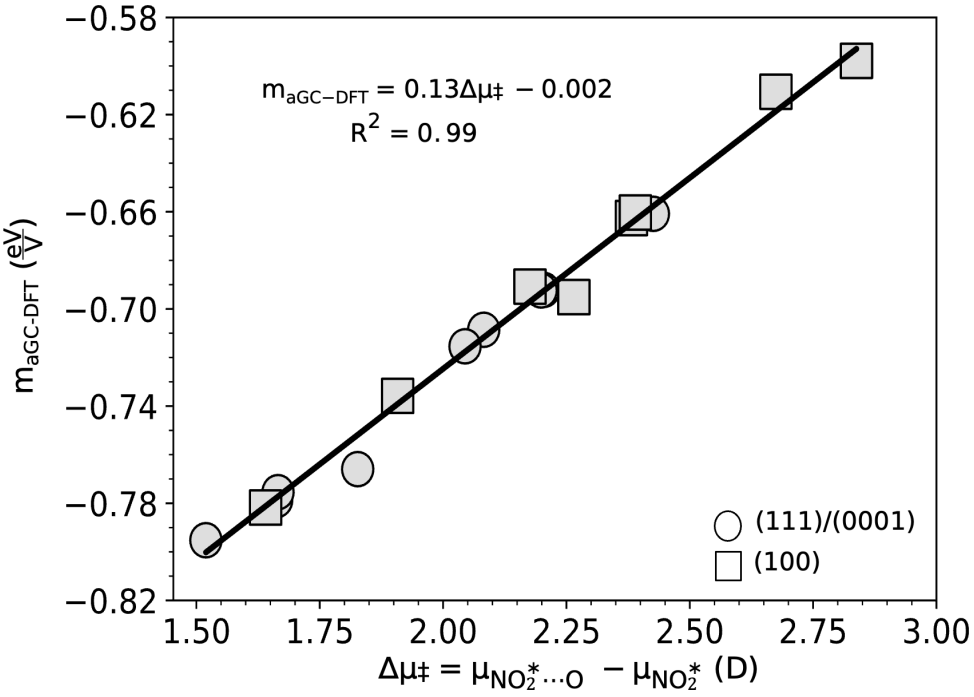

Figure 4: The shift in dipole moment for NO_3^- adsorption versus the electrosorption valency ($m_{aGC\text{-}DFT}$) computed from the analytical GC-DFT method across pure metals and SAAs. The electrosorption valency was computed as the slope of the line-of-best fit to the analytical GC-DFT data.

Table 4: Electrosorption valency, shift in dipole moment, and charge transfer from to NO_3^- to the surface upon adsorption on metals and SAAs (units: eV/V, Debey (D), unitless)

	Electrosorption Valency	$\Delta\mu_{NO_3^*}$	$\Delta q_{NO_3^*}$
$Rh_1Cu(111)$	–0.692	0.459	0.712
$Ni_1Cu(111)$	–0.709	0.434	0.688
$Ru_1Cu(111)$	–0.715	0.426	0.732
$Pd_1Cu(111)$	–0.661	0.505	0.633
Cu(111)	–0.692	0.458	0.638
Pd(111)	–0.766	0.380	0.715
Rh(111)	–0.779	0.346	0.785
Ru(0001)	–0.795	0.316	0.764
Ni(111)	–0.775	0.347	0.748
$Rh_1Cu(100)$	–0.663	0.496	0.704
$Ni_1Cu(100)$	–0.660	0.498	0.666
$Ru_1Cu(100)$	–0.691	0.453	0.726
$Pd_1Cu(100)$	–0.598	0.591	0.608
Cu(100)	–0.611	0.557	0.613
Pd(100)	–0.695	0.472	0.689
Rh(100)	–0.782	0.342	0.781
Ni(100)	–0.736	0.397	0.719

Table 5: Symmetry factor, shift in dipole moment, and charge transfer for NO_3* dissociation over metals and SAAs (units: eV/V, Debye (D), unitless)

Metal (facet)	Symmetry Factor	$\Delta\mu_{\ddagger}$
$Rh_1Cu(111)$	–0.104	–0.743
$Ni_1Cu(111)$	–0.184	–1.324
$Ru_1Cu(111)$	–0.109	–0.784
$Pd_1Cu(111)$	–0.205	–1.490
Cu(111)	–0.175	–1.268
Pd(111)	–0.163	–1.152
Rh(111)	–0.168	–1.205
Ru(0001)	–0.144	–1.032
Ni(111)	-	-
$Rh_1Cu(100)$	–0.152	–1.106
$Ni_1Cu(100)$	–0.139	–1.027
$Ru_1Cu(100)$	–0.106	–0.777
$Pd_1Cu(100)$	-	-
Cu(100)	–0.123	–0.887
Pd(100)	–0.152	–1.054
Rh(100)	–0.059	–0.413
Ni(100)	-	-

Density of States Calculations

Partial Density of States (pDOS) calculations were performed in VASP using the tetrahedron method (ISMEAR=-5) with an 11×11×1 Gamma-centered k-point grid. Gaussian smoothing was applied to the DOS data to obtain continuous, smooth distributions. The d-band filling was calculated relative to the Fermi level using eq. (6).

$$f_d = \frac{\int_{-\infty}^{0} \rho(\varepsilon) d\varepsilon}{\int_{-\infty}^{\infty} \rho(\varepsilon) d\varepsilon} \tag{6}$$

Derivations for the aGC-DFT Model

We can start with the most general form of the aGC-DFT model to approximate the change in grand free energy, $\Delta\Phi$, between any two states, χ_1 and χ_2. Shown in eq. 7, n_e represents the number of electrons/protons transferred within a PCET reaction step. We refer the reader to the main text for descriptions of each term within this expression.

$$\begin{aligned}\Delta\Phi(U) = \Delta\Phi(U_{\chi_2}, U_{\chi_1}) - \frac{1}{2}\frac{\varepsilon A}{d}\left((U'_{\chi_2})^2 - (U'_{\chi_1})^2\right) \\ + \mu_{\chi_2}\left(\frac{U'_{\chi_2}}{d}\right) - \mu_{\chi_1}\left(\frac{U'_{\chi_1}}{d}\right) + \frac{\alpha_{\chi_2}}{2}\left(\frac{U'_{\chi_2}}{d}\right)^2 - \frac{\alpha_{\chi_1}}{2}\left(\frac{U'_{\chi_1}}{d}\right)^2 \pm n_e U\end{aligned} \tag{7}$$

To compute the first-order derivative with respect to the U, we first need to substitute in $U'_\chi = U - U_\chi$, where $U_\chi = U_0 + \frac{\mu_\chi}{\varepsilon A}$, shown in eq. (8).

$$\begin{aligned}\Delta\Phi(U) = \Delta\Phi(U_{\chi_2}, U_{\chi_1}) + \frac{2\Delta\mu}{d}(U - U_0) - \frac{3}{2\varepsilon A d}(\mu_{\chi_2}^2 - \mu_{\chi_1}^2) \\ + \frac{\alpha_{\chi_2}\mu_{\chi_2}^2 - \alpha_{\chi_1}\mu_{\chi_1}^2}{2(\varepsilon A d)^2} - \frac{\Delta\alpha\mu}{2\varepsilon A d^2}(U - U_0) - \frac{\Delta\alpha}{2d^2}(U - U_0)^2 \pm U n_e\end{aligned} \tag{8}$$

We can then take the derivate of eq. (8) with respect to U, shown in eq (9). We write the derivative in this format to demonstrate negligible polarizability effects yield a linear

potential dependence as a function of $\Delta\mu$.

$$\frac{\partial \Delta\Phi(U)}{\partial U} = \frac{2\Delta\mu}{d} + \frac{\alpha_{\chi_2}}{d^2}\left(U - U_0 - \frac{\mu_{\chi_2}}{\varepsilon A}\right) - \frac{\alpha_{\chi_1}}{d^2}\left(U - U_0 - \frac{\mu_{\chi_1}}{\varepsilon A}\right) \pm n_e \tag{9}$$

The electrosorption valency for the NO_3^* adsorption ($\chi_1 = *, \chi_2 = NO_3^*$) is derived by observing that $\alpha_* = 0$ and $n_e = -1.0$. Additionally, the symmetry factor for NO_3^* dissociation ($\chi_1 = NO_3^*$, $\chi_2 = \ddagger$) is derived by setting $n_e = -0.0$ because there is no PCET during the dissociation.

We can also use eq. (8) to derive an expression for the error in neglecting EDL effects for both NO_3^* adsorption and NO_3^* dissociation, shown in eq. (10). The first term in the error expression indicates the capacitive energy to charge the double layer, the second term accounts for dipole-field interactions, and the remaining terms account for induced dipole-filed interactions. For derivation purposes, we can neglect polarizability effects and derive eq. (11). However, the errors presented in-text are computed with polarizability effects, albeit small.

$$\Sigma_{ABS} = |\frac{2\Delta\mu}{d}(U-U_0) - \frac{3}{2\varepsilon A d}(\mu_{\chi_2}^2 - \mu_{\chi_1}^2) + \frac{\alpha_{\chi_2}\mu_{\chi_2}^2 - \alpha_{\chi_1}\mu_{\chi_1}^2}{2(\varepsilon A d)^2} - \frac{\Delta\alpha\mu}{2\varepsilon A d^2}(U-U_0) - \frac{\Delta\alpha}{2d^2}(U-U_0)^2| \tag{10}$$

$$\Sigma_{ABS} = |\frac{2\Delta\mu}{d}(U - U_0) - \frac{3}{2\varepsilon A d}(\mu_{\chi_2}^2 - \mu_{\chi_1}^2)| \tag{11}$$

Rewriting eq. (11) as eq. (12) because $\Sigma_{ABS} = \Sigma_{SQ}$, we can compute the potential at which the error is minimized, $U_{\min}$, by taking the derivative of eq. (12) and setting it to zero. The full expression is shown in eq. (13)

$$\Sigma_{SQ} = \sqrt{\left(\frac{2\Delta\mu}{d}(U - U_0) - \frac{3}{2\varepsilon A d}(\mu_{\chi_2}^2 - \mu_{\chi_1}^2)|\right)^2} \tag{12}$$

$$U_{min} = \frac{3}{4\varepsilon A}(\mu_{\chi_1} + \mu_{\chi_2}) + U_0 \tag{13}$$

References

(1) Darby, M. T.; Sykes, E. C. H.; Michaelides, A.; Stamatakis, M. Carbon Monoxide Poisoning Resistance and Structural Stability of Single Atom Alloys. *Topics in Catalysis* **2018**, *61*, 428–438.

(2) Lange, N. A. *Lange's handbook of chemistry*, 16th ed.; McGraw-Hill standard handbooks; McGraw-Hill Education: New York, 2013.

(3) Sander, R. Compilation of Henry's law constants (version 4.0) for water as solvent. *Atmospheric Chemistry and Physics* **2015**, *15*, 4399–4981, Publisher: Copernicus GmbH.

(4) Agrawal, N.; Wong, A. J.-W.; Maheshwari, S.; Janik, M. J. An efficient approach to compartmentalize double layer effects on kinetics of interfacial proton-electron transfer reactions. *Journal of Catalysis* **2024**, *430*, 115360.